Fernández-Torrijos, M., Sobrino, C., Almendros-Ibáñez, J. A., Marugán-Cruz, C., & Santana, D. (2019). Inverse heat problem of determining unknown surface heat flux in a molten salt loop. International Journal of Heat and Mass Transfer, 139, 503-516.

doi: https://doi.org/10.1016/j.ijheatmasstransfer.2019.05.002

Inverse heat problem of determining unknown surface heat flux in a molten salt loop

M. Fernández-Torrijos[a,*], C. Sobrino[a], J. A. Almendros-Ibáñez[b,c], C. Marugán-Cruz[a], D. Santana[a]

[a] *Universidad Carlos III de Madrid, ISE Research Group, Thermal and Fluid Engineering Department, Avda. de la Universidad 30, 28911 Leganés, Madrid, Spain*
[b] *E.T.S. de Ingenieros Industriales de Albacete, Dpto. de Mecánica Aplicada e Ingeniería de Proyectos, Castilla La Mancha University, Campus universitario s/n, 02071, Albacete, Spain*
[c] *Renewable Energy Research Institute, Section of Solar and Energy Efficiency, C/ de la Investigación s/n, 02071, Albacete, Spain*

Abstract

Inverse heat transfer problems typically rely on temperature measurements for estimating unknown boundary heat flux, such as that in the water tubes of steam boilers or central receivers in solar tower power plants. In this work, an experimental facility consisting of a molten salt loop that simulates a tube of a solar tower receiver is presented to obtain the outer tube surface temperatures under solar tower power plant operating conditions. The external surface of the pipe in the test section is heated in a controlled manner with an induction heater, which provides a very high nonuniform heat flux. An inverse thermal method has been applied to obtain the incident heat flux onto the receiver tube from the outer surface temperature measurements. To solve the inverse problem, a transient two-dimensional numerical model of a circular pipe flowing molten nitrate salt and subjected to a nonhomogeneous circumferential heat flux has been developed. The heat flux calculation with the inverse method is in accordance with the heat flux estimation based on the calibration of the induction heater. A good agreement between the experimental and calculated temperatures is observed. Furthermore, the deflection of the tube caused by

*Corresponding author. Tel.: +34 916246224
Email address: ftorrijo@ing.uc3m.es (M. Fernández-Torrijos)

the nonhomogeneous heat flux is measured and is compared to the deflection calculated from the radial temperature profile from the inverse problem solution, and a good agreement between both results is observed.

Keywords: Inverse heat conduction problem, Inductor coil, Central receiver, Tube bending.

---

1. Introduction

Concentrating Solar Power (CSP) with Thermal Energy Storage (TES) is a key technology to contribute to increasing the penetration of renewable energy in the electricity mix and to the reduction of greenhouse gas emissions, since it increases the flexibility of the electricity system avoiding the need of fossil fuel back up. A typical CSP plant consist of: i) a solar concentrator, where the solar radiation is reflected; ii) the receiver, where the solar radiation is transferred to the heat transfer fluid (HTF); iii) the TES system, where the thermal energy is stored; iv) the heat exchangers, where the heat is transferred from the HTF of the storage system to the working fluid of the power block and v) the power block, that converts the thermal energy into electricity. The main CSP systems are linear Fresnel reflectors, central receivers (power towers), parabolic trough and parabolic dish systems. A linear Fresnel consists of a large number of mirrors in parallel rows plane or slightly curved that reflect the sunlight to a pipe above. Power tower or central receiver systems utilize sun-tracking mirrors called heliostats to focus sunlight onto a receiver at the top of a tower. In a parabolic trough CSP system, radiation is concentrated by parabolically curved, trough-shaped reflectors onto a receiver pipe running along about a meter above the curved surface of the mirrors. A Parabolic dish system consists of a parabolic-shaped point focus concentrator in the form of a dish that reflects solar radiation onto a receiver mounted at the focal point. Today's most advanced CSP systems are central receivers integrated with 2-tank TES, working with nitrate molten salt both in the receiver and in the storage system and delivering thermal energy at 565°C for integration with conventional steam-Rankine power cycles. Receiver tubes can reach very high temperatures of 650-750°C and are exposed to a nonuniform solar flux that can exceed 1.0 MW/m^2. This results in an uneven temperature distribution in the circumferential direction, resulting in thermal stresses (Marugán-Cruz et al., 2016) and deflections in the receiver tubes that can reduce their service life. In central external receivers, the flux distribution is designed to heat the salt from 290°C to 565°C while keeping the strain and corrosion in the receiver tubes within allowable limits. The receiver temperatures are used as inputs to some of the flux management systems of a commercial plant to make it operate within these limits. Thermocouples are installed on the back (non-illuminated) wall of the receiver tubes (Pacheco, 2002). The back-wall thermocouples provide information on changes much more quickly than the outlet salt thermocouple because they measure receiver panel information, not just the outlet conditions (Smith and Chavez, 1992). Moreover, since the tube wall is relatively small and the thermocouple is placed on the back of the tube (away from the incident flux), the temperature measurement should represent the bulk salt temperature within the tube at that point (Smith and Chavez, 1992).

The phenomena that occur in different subsystems of a molten salt CSP plant are reproduced in lab-scale molten salt loops to study them under controlled conditions. Some experimental works measured the convection coefficient for the internal flow of molten salt in a pipe at a high Reynolds number that is characteristic of real receivers ($>10^4$). Typically, an electrical heater heats the pipe in the test section, providing uniform heat fluxes in the range of 200-400 kW/m^2 (Yang et al., 2012; Jianfeng et al., 2013a,b; Kim et al., 2018). Uniform heat transfer can also be achieved through a heat exchanger with another fluid (Yu-ting et al., 2009; Du et al., 2017). In very few experimental facilities, the heat flux is applied unilaterally to the testing tube. For instance, Xiangyang et al. (2014) measured the Nusselt number of a molten salt in a pipe with a nonuniform heat flux that was considerably higher on one of its sides. They found that the Nusselt number of the side with the highest heat flux was lower than that of the side with the lowest heat flux.

To produce a higher heat flux similar to that of central receivers, the pipe can be heated in a small area using an inductor. The inductor includes a copper coil and a magnetizer, also called an electromagnetic flux concentrator. As high-frequency alternating current flows in the coil, a high eddy current is induced in the surface layer of the metal piece, which leads to a rapid increase in the temperature of the surface layer (Zhu et al., 2018). When the concentrator is properly designed, a high heating rate and uniform temperatures of the metal piece can be achieved (Gao et al., 2016). When using this heating method, a high wall temperature of the tube is reached. Kruizenga et al. (2014) employed an inductor to uniformly heat the external surface of a 1 m long test section pipe in a pumped-salt test loop where molten nitrate salt circulated to simulate a solar receiver. In particular, the internal surface of the pipe was maintained at a temperature of approximately 670°C to study the decomposition of the salt. However, the determination of this temperature is problematic because it cannot be directly measured and the power applied by the inductor heater cannot be directly taken as the thermal power input of the pipe due to the losses.

The determination of the heat flux and subsequently the internal surface temperature of the receiver pipe from the measurement of the external surface temperature, which can be accomplished in practice, is of crucial interest in both commercial plants and lab-scale installations. The direct measurements of heat flux on commercial plants is very difficult for a cylindrical receiver, and computer simulations are used instead (Pacheco, 2002).

Inverse heat conduction problems have generally been associated with the estimation of an unknown boundary heat flux by using temperature measurements (Özisik and Orlande, 2000). This is the opposite of a classical direct heat conduction problem where the boundary heat flux is given while the temperature field is determined. Several techniques for solving the inverse problem have been developed, for example, the conjugate gradient method, the method of fundamental solutions, linear least-squares methods, analytical methods and genetic algorithms (Alifanov, 1994; Taler and Duda, 2006). In particular, an inverse heat transfer analysis has previously been applied (Yang et al., 2013) to estimate the unknown time-dependent inner-wall heat flux of a hollow cylinder from the knowledge of the temperatures within the medium at different radial positions. The temperature data were simulated to represent temperature measurements with the objective of evaluating the conjugate gradient method proposed to solve the inverse heat transfer problem. Su and Silva-Neto (2001) applied the conjugate gradient method to solve the radial and circumferential transient dependence of source strength in cylindrical rods. Lu et al. (2010) applied an inverse heat conduction problem to obtain the unknown transient fluid temperatures near the inner wall of a pipe elbow with thermal stratification from simulated outer surface temperature measurements. Besides these numerical solution techniques, analytical methods have been applied to solve inverse heat conduction problems. For instance, Cattani et al. (2015) applied the Quadrupole Method coupled to the Truncated Singular Value Decomposition Approach to estimate the local convective heat transfer coefficient on the internal wall surface of a pipe. Additionally, Maillet et al. (1991) applied the least-squares method coupled to the analytical solution of the 2-D temperature field to the measurement of a heat transfer coefficient on a cylinder. Inverse heat transfer methods have been successfully applied to different technological fields. Taler et al. (2009) developed a heat tubular-type instrument (flux-tube) to measure the heat flux to water walls of combustion chambers based on the inverse heat conduction problem. Thus, they calculated the heat flux absorbed by the walls from surface temperature measurements (Taler et al., 2014). The temperature history measured in two-phase boiling experiments during and following the critical heat flux were used in the solution of the two-dimension inverse heat transfer problem to estimate the wall temperatures and wall heat fluxes in water-cooled reactors (Duarte et al., 2018). Perakis and Haidn (2019) applied a 3D inverse method for estimating the time- and spatially resolved heat flux distribution at the hot gas wall of rocket combustors. Yadav et al. (2018) developed a two-thermocouple model especially suitable to be applied to time-varying high heat flux applications such as nuclear reactor containments, reactor pressure vessels, furnaces, and jet heating/cooling etc. Liu et al. (2018) obtained an analytical inverse heat transfer solution which can be used to calculate surface heat flux in temperature-sensitive coating measurements in high-enthalpy hypersonic wind tunnels. An inverse heat transfer was also applied to the diagnosis of the lateral refractory brick wall of a melting furnace (Hafid and Lacroix, 2017), allowing to predict the time-varying thickness of the protective bank that covers the inner lining of the furnace wall, the thermal contact resistance between the inner lining and the protective bank and the possible erosion of the refractory brick wall. Concerning the solar technology field, inverse heat transfer methods have been applied to predict the heat flux distribution on a flat plate receiver in a solar Concentrating Photovoltaic system using non-intrusive temperature measurement obtained with an IR camera (Reddy et al., 2018).

In the present paper, an inverse heat transfer method is applied to calculate the heat flux at the outer surface of a pipe conducting molten nitrate salt from outer surface temperature measurements. The measurements were performed in a molten salt loop that simulates the receiver of a solar tower. The external surface of the pipe in the measurement area is heated using an inductor, which provides a very high nonuniform heat flux. Once the heat flux is calculated from the outer surface temperature measurements, the radial temperature profile in the pipe wall is obtained. Additionally, the deflection of the tube caused by the unilateral heat flux is measured, and it is compared to the deflection calculated from the radial temperature profile. Experimental measurements of the outer surface temperature of a receiver tube under solar tower power plant operating conditions have not been reported in the literature before, which can be useful for the validation of tubular external molten salt receiver numerical models. Moreover, for the first time, an inverse heat transfer method has been applied to obtain the incident heat flux onto a solar receiver, which is of interest in both commercial plants and lab-scale installations.

2. Experimental setup

The experiments were performed in a molten salt (60% $NaNO_3$/40% KNO_3) test loop (Figure 1) that consists of a cylindrical molten salt tank, a pump, a pressure sensor, the test section and a flow meter. The total length of the loop is greater than 12 m. The 600 l tank is made of AISI316 and is heated by an electrical furnace. The temperature of the molten salt in the tank is controlled to maintain it between 300 °C and 500 °C. A high-temperature pump coupled to an electric motor equipped with a variable-frequency drive allows varying the flow rate through the molten salt loop. The tank is connected to a 304 stainless steel pipe, with a 5.2 cm inner diameter and 4 mm thickness, through which the molten salt circulates, reaching Reynolds numbers in the range of $4 \cdot 10^4$-$2 \cdot 10^5$. An ultrasonic flow meter allows measuring the flow rate at the test section. The pipe is wrapped with electrical heaters and insulated in the whole loop except in the 0.5 m test section, where an induction heat generator provides a high heat flux that is applied to a small rectangular region of the tube surface such that the inductor reproduces the nonuniform heating conditions of the receiver in a central tower plant. The induction heater has an output power of 6 kW and output frequency range of 270-450 kHz. The inductor coil is provided with a magnetic flux concentrator that, when properly designed, produces a high heating rate and uniform temperature of the metal piece. To ensure a satisfactory heating process (Gao et al., 2016), the distance between the coil and the heating surface was fixed to 7 mm, the working frequency of the inductor was 300 kHz, and a rectangular coil of 100 mm x 7 mm with a magnetic flux concentrator of 4 mm in width, 4 mm in height, and 100 mm in length was used, as shown in Figure 2.

The total electric power provided by the induction heater was 4 kW_e in the experiments conducted in the molten salt loop. The heat flux reaching the tube was applied in a rectangular area of 100 mm x 15 mm, which corresponds to the area occupied by the coil and the magnetic flux concentrator. Thus, the maximum heat flux that could reach the external wall of the pipe would be 2.67 MW/m^2. Since the induction coil needs to be chilled with water, part of the heat flux generated by the induction heater is transferred to the stream of water flowing through the coil. Therefore, it is difficult to accurately determine the heat flux that reaches the external wall of the pipe knowing the total electric power of the induction heater. In this work, some experiments to calibrate the induction heater for different electric powers (i.e., 3, 5 and 7 kW_e) were conducted to determine the percentage of the electrical power of the induction heater that is effectively transferred to the tube. With this aim, a 1.5 m long tube made of the same material and with the same inner and outer diameters as those of the tube used in the molten salt loop was heated by the induction coil. The tube was placed vertically, and it was closed at the bottom end and externally insulated using a mineral wool. Then, it was filled with water, and thermocouples were installed to measure the temperature of the water inside the tube and the temperature of the outer surface of the tube wall. Additionally, the flow rate and the inlet and outlet temperatures of the cooling water flowing through the induction coil were measured. According to these measurements, we concluded that approximately 35% of the inductor electrical power is transferred to the inductor cooling water and that only 40% is converted to thermal energy that reaches the tube and heats the wall and the water contained in it. Hence, this calibration experiment indicates that given this 40% efficiency, for the experimental conditions presented in this paper (inductor electrical power of 4 kW_e applied to a 15 x 100 mm area), the heat flux applied to the external surface of the tube is approximately 1 MW/m^2. However, to more accurately predict the heat flux incident on the test section, an inverse algorithm based on the outer surface temperature measurements has been proposed in this work.

[Figure 1 about here.]

[Figure 2 about here.]

To measure the temperature of the external surface of the pipe along the angular position, skin thermocouples were used. They consist of a sheath K-type thermocouples embedded in a steel plate to facilitate the welding of the thermocouple to the pipe (see Figure 4). A total of 7 thermocouples were used: 5 thermocouples welded to the outer surface of the pipe in different positions along the circumferential direction at the axial position corresponding to the center of the coil, and 2 thermocouples inside the pipe at $r = 0$ to measure the bulk salt temperature, located at $z = -0.21$ m and $z = 0.21$ m as shown in Figure 3. In addition, the installation has four sheath K-type thermocouples inside the tank to control the temperature of the salt between 300 °C and 500 °C and a thermocouple welded to the tank wall to prevent the temperature from exceeding 550 °C. For data acquisition, National Instruments' 9219 universal analog input acquisition cards were used. This module has 4 channels and has the advantage of having interchannel isolation such that each channel is isolated from all other channels and other noninsulated components to reject interchannel noise and electromagnetic noise from the induction heater.

Moreover, thermal images were taken with an IR camera (Optris PI640 with O15 telephoto lens) during the experiments to study the deformation of the tube due to the nonuniform heat flux, which results in an uneven temperature distribution, as shown in the left picture of Figure 4. The right picture of Figure 4 shows the position of the pipe with uniform tube temperature when the molten salt is flowing through the pipe and the induction coil is not heating the tube. Comparing both pictures and considering that the green rectangle corresponds to the distance between the induction coil and the pipe, the tube bending due to the nonuniform heat flux provided by the induction heater is appreciated. The analysis of the IR camera images over time provided the displacement of the tube with an error of ± 0.2 mm because the size at a single pixel at the object level was 0.4 mm.

[Figure 3 about here.]

[Figure 4 about here.]

3. Numerical modeling

3.1. Direct problem

3.1.1. Heat conduction in pipe wall

In this work, a transient numerical model has been developed to compare the experimental measurements with the numerical results. The heat transfer problem of a circular pipe subjected to a nonhomogeneous heat flux in the circumferential direction while a molten-salt stream is flowing through the pipe is considered. For simplicity, the heat transfer problem along the molten-salt flow is not calculated, and the heat exchange between the molten-salt stream and the pipe wall is solved using Petukhov's correlation. The physical properties of the salt, which are known functions of temperature (Zavoico, 2001), were calculated at the molten-salt inlet temperature. To solve the heat transfer problem along the pipe wall, a homogeneous heat flux in the axial direction was considered to develop a two-dimensional model of the pipe. Thermal conduction in axial direction was neglected, as negligible temperature difference was shown between one thermocouple placed at the axial position of the center of the coil and another thermocouple at $z = 27$ mm, being both of them at the same angular position. Therefore, the cross section studied in this work, which was placed at the center of the coil, was not affected by the conductive axial heat losses that occurs at the two ends of the heated part, as the temperature field along the length of the induction heater was shown to be uniform. During the postprocessing of the results, it was verified that the heat flux in axial direction computed from the temperature measurements was three order of magnitude lower compared to the total heat flux in radial and circumferential directions, for a cross section placed at the center of the coil. Therefore, heat is transferred by conduction in the radial and circumferential directions along the pipe according to the heat diffusion equation.

$$\rho\, c_p \frac{\partial T(r,\theta,t)}{\partial t} = \frac{k}{r}\frac{\partial}{\partial r}\left(r\,\frac{\partial T(r,\theta,t)}{\partial r}\right) + \frac{k}{r^2}\frac{\partial^2 T(r,\theta,t)}{\partial \theta^2} \tag{1}$$

where T is the wall temperature, ρ is the wall density, c_p is the wall specific heat, and k is the wall conductivity. The inner wall of the pipe is in contact with the molten salt, so its thermal boundary condition is set to a convective heat transfer condition. The outer wall of the pipe is in contact with the atmosphere, so its thermal boundary condition is set to a mixed convective and radiative heat transfer condition. The initial temperature of the pipe is uniform along the circumferential direction and, for simplicity, it was considered to be uniform in radial direction, as the temperature difference between inner and outer surfaces was approximately 1°C due to the radiative and convective losses to the ambient. Therefore, the initial temperature was assumed to be the measured temperature at $r = r_o$ at the beginning of the experiment. Hence, the boundary and initial conditions of the problem are expressed as follows:

$$-k\frac{\partial T(r,\theta,t)}{\partial r} = h_i \; (T_s - T(r,\theta,t)) \text{ at } r = r_i \tag{2}$$

$$-k\frac{\partial T(r,\theta,t)}{\partial r} = h_{conv+rad}(\theta,t) \; (T(r,\theta,t) - T_\infty) - q_{ind}(\theta,t) \text{ at } r = r_o \tag{3}$$

$$\frac{\partial T(r,\theta,t)}{\partial \theta} = 0 \text{ at } \theta = 0, \pi \tag{4}$$

$$T(r,\theta,t) = T_{ini} \quad \text{for } t = 0 \tag{5}$$

where r_i and r_o are the inner and outer pipe radii, respectively; T_s and T_∞ are the temperatures of the molten salt and surroundings, respectively; h_i is the convective heat transfer from the molten salt to the inner surface of the wall; and $h_{conv+rad}$ is the mixed convective and radiative heat transfer from the outer surface of the pipe to the atmosphere. θ is the circumferential coordinate, which has its origin at the front part of the pipe, facing the induction coil, as shown in Figure 5, and q_{ind} is the heat flux from the induction heater applied to the external wall of the pipe, where q_{ind} was considered to be positive when the heat flux is coming from the induction heater to the pipe (see Figure 5). Notice that only half of the tube was simulated due to symmetry. For the experiments developed in this work, q_{ind} was assumed to be uniform in the area of the pipe facing the induction coil and the magnetic flux concentrator (-15° $\leq \theta \leq$ 15°), while the area not facing the coil did not receive heat flux from the induction heater (see Figure 5).

$$q_{ind}(\theta,t) = \begin{cases} q_{ind}(t) & \text{if } \theta \le 15^\circ \\ 0 & \text{if } \theta > 15^\circ \end{cases} \tag{6}$$

The convection coefficient h_i was calculated using the correlation proposed by Petukhov (1970) for turbulent flow, while $h_{conv+rad}$ was obtained as follows:

$$h_{conv+rad}(\theta,t) = h_\infty + \varepsilon\,\sigma_r\,(T(r,\theta,t) + T_\infty)\,(T^2(r,\theta,t) + T_\infty^2) \tag{7}$$

where h_∞ is the convection coefficient from the outer surface of the pipe to the atmosphere, σ_r is the Stefan-Boltzmann constant, and ε is the AISI304 surface emissivity. The emissivity (ε) of the outer wall surface was measured with an infrared camera, and a value of 0.32 was obtained. The convection coefficient (h_∞) was calculated using Churchill's correlation for horizontal cylinders (Churchill and Chu, 1975).

[Figure 5 about here.]

Heat conduction in the wall was considered to be two-dimensional to take the temperature variations along the radius and the circumferential direction of the wall into account. An explicit finite difference method was used to solve the transient heat conduction equation. The energy balance method was applied by dividing the wall into nodes in the azimuthal direction ($\Delta\theta$) and radial direction (Δr). The temperature at the midpoint of cell (i,j) is called $T_{i,j}$. The geometry of the cell is a circular trapezoid of sides Δr and $r\,\Delta\theta$, as shown in Figure 6.

[Figure 6 about here.]

The thermal coupling between the cells is modeled by thermal conductances. The conductances in the circumferential direction between cells $(i-1,j)$ and (i,j) and cells (i,j) and $(i+1,j)$ are

$$K_{i-0.5,j} = K_{i+0.5,j} = \frac{L\,\Delta r\,k}{r_j\,\Delta\theta} \quad \text{for } i = 1\ldots N_k \tag{8}$$

The general expressions for conductance that are valid for the inner nodes along the radial direction are

$$K_{i,j-0.5} = \frac{L\,k\Delta\theta}{\ln \dfrac{r_j}{r_{j-1}}} \quad \text{for } j = 2\ldots M_k \tag{9}$$

$$K_{i,j+0.5} = \frac{L\,k\Delta\theta}{\ln \dfrac{r_{j+1}}{r_j}} \quad \text{for } j = 1\ldots M_k - 1 \tag{10}$$

The inner cell along the radial direction ($j = 1$) is in contact with the molten salt; thus, the conductance results in

$$K_{i,0.5} = \frac{L}{\dfrac{1}{\Delta\theta\, r_i\, h_i} + \dfrac{1}{\Delta\theta\, k} \ln \dfrac{r_1}{r_i}} \tag{11}$$

The outer cell along the radial direction ($j = M_k$) is exposed to the atmosphere; thus, the conductance results in

$$K_{i,M_k+0.5} = \frac{L}{\dfrac{1}{\Delta\theta\, k} \ln \dfrac{r_o}{r_{M_k}} + \dfrac{1}{\Delta\theta\, r_o\, h_{(conv+rad)_i}}} \tag{12}$$

Figure 6 shows a scheme of the incident/outgoing heat flows associated with an internal cell. The heat flows through the left ($Q_{i-0.5,j}$) and right ($Q_{i+0.5,j}$) boundaries of a cell are defined by the following expressions:

$$Q_{i-0.5,j}(t) = K_{i-0.5,j}\,(T_{i-1,j}(t) - T_{i,j}(t)) \tag{13}$$

$$Q_{i+0.5,j}(t) = K_{i+0.5,j}\,(T_{i,j}(t) - T_{i+1,j}(t)) \tag{14}$$

The heat flows through the inner ($Q_{i,j-0.5}$) and outer ($Q_{i,j+0.5}$) radius boundaries are expressed as follows:

$$Q_{i,j-0.5}(t) = K_{i,j-0.5}\,(T_{i,j-1}(t) - T_{i,j}(t)) \tag{15}$$

$$Q_{i,j+0.5}(t) = K_{i,j+0.5}\,(T_{i,j}(t) - T_{i,j+1}(t)) \tag{16}$$

The energy conservation of the wall is solved to obtain the temperature field of the wall

$$\rho\, c_p\, V\, \frac{\partial T(r,\theta,t)}{\partial t} = Q_{i-0.5,j}(t) - Q_{i+0.5,j}(t) + Q_{i,j-0.5}(t) - Q_{i,j+0.5}(t) \tag{17}$$

The outer cell along the radial direction ($j = M_k$) is exposed to the induction heat flux; thus, the energy conservation of the wall results in

$$\rho\, c_p\, V\, \frac{\partial T(r,\theta,t)}{\partial t} = Q_{i-0.5,j}(t) - Q_{i+0.5,j}(t) + Q_{i,M_k-0.5}(t) - Q_{i,M_k+0.5}(t) + \Delta\theta\, r_o\, L\, q_{ind}(\theta,t) \tag{18}$$

where $V = \Delta\theta\, r_j\, \Delta r\, L$ is the cell volume. $L = 1$ in Equations (8)-(12) and Equations (17)-(18) because when solving a two-dimensional heat transfer problem, a unit depth cell is assumed.

[Table 1 about here.]

3.1.2. Deflection of the pipe

The pipe wall is exposed to tension and compression in its different parts due to the nonuniform temperature distribution along the circumferential direction, which results in a moment that causes bending of the pipe. The tube is 4.33 m long between supports (L_T), and the center of the induction coil, which provides the heat flux, is positioned at 2.63 m from the first support, as shown in Figure 7. Deflection $\delta(z,t)$ and rotation $\Theta(z,t)$ are considered to be zero at the ends, but the tube can elongate freely.

$$\delta(z,t) = 0 \quad \text{for } z = 0, L_T \tag{19}$$

$$\Theta(z,t) = 0 \quad \text{for } z = 0, L_T \tag{20}$$

[Figure 7 about here.]

The moment induced by the circumferential temperature gradient $M_T(t)$ is expressed as

$$M_T(t) = 2\, E\, \alpha \int_0^{\pi} \int_{r_i}^{r_o} T(r,\theta,t)\, r^2 \cos\theta\, dr\, d\theta \tag{21}$$

where E is the Modulus of Elasticity, and α is the thermal expansion coefficient. The relation between the deflection and the moment $M(z,t)$ is expressed as (Gere, 2004)

$$\frac{d^2(\delta(z,t))}{dz^2} = \frac{M(z,t)}{E\, I} \tag{22}$$

where I is the moment of inertia of a circular pipe $\frac{\pi}{4}(r_o^4 - r_i^4)$. To obtain the deflection and bending moment from Equation (22), the reactions and moments at the supports of the pipe are obtained

$$R_a + R_b = 0 \tag{23}$$

$$M_a - R_a \cdot L_T - M_b = 0 \tag{24}$$

The bending moment along the length of the pipe between supports is obtained taking the moment equilibrium at point x

$$M(z,t) = -M_a + R_a \cdot z \quad \text{for } 0 \le z < L_1 \tag{25}$$

$$M(z,t) = -M_a + R_a \cdot z + M_T(t) \quad \text{for } L_1 \le z < L_2 \tag{26}$$

$$M(z,t) = -M_a + R_a \cdot z \quad \text{for } L_2 \le z \le L_T \tag{27}$$

where L_1 and L_2 are the lengths from the first support to the beginning and end of the induction coil, respectively. Substituting Equations (25)-(27) into Equation (22) and integrating and imposing the boundary conditions, the deflection of the pipe can be expressed as

$$\delta(z,t) = \frac{M_T(t)}{E\,I}\left(\frac{(L_1 - L_2)\,(L_1 + L_2 - L_T)}{L_T^3}\,z^3 - \frac{(L_1 - L_2)\,(3L_1 + 3L_2 - 4L_T)}{2L_T^2}\,z^2\right) \quad \text{for } 0 \le z < L_1 \tag{28}$$

$$\delta(z,t) = \frac{M_T(t)}{E\,I}\left(\frac{(L_1 - L_2)\,(L_1 + L_2 - L_T)}{L_T^3}\,z^3 + \left(1 - \frac{(L_1 - L_2)\,(3L_1 + 3L_2 - 4L_T)}{L_T^2}\right)\frac{z^2}{2} - L_1\,z + \frac{L_1^2}{2}\right) \quad \text{for } L_1 \le z < L_2 \tag{29}$$

$$\delta(z,t) = \frac{M_T(t)}{E\,I}\left(\frac{(L_1 - L_2)\,(L_1 + L_2 - L_T)}{L_T^3}\,z^3 - \frac{(L_1 - L_2)\,(3L_1 + 3L_2 - 4L_T)}{2L_T^2}\,z^2 + (L_2 - L_1)z + \frac{L_1^2 - L_2^2}{2}\right) \quad \text{for } L_2 \le z \le L_T \tag{30}$$

3.2. Inverse problem

In this work, an inverse algorithm is proposed to obtain the unknown time- and space-dependent heat flux received by the pipe from the knowledge of temperature measurements of the external wall of the pipe. For solving the inverse heat conduction problem, the conjugate gradient method with adjoint problem for parameter estimation was used (Özisik and Orlande, 2000). The formulation consists of the direct problem, which was explained in the previous section; the sensitivity problem; the adjoint problem; and the gradient equations. For solving the inverse problem, the unknown function q_{ind} was parameterized

$$q_{ind} = P \cdot C(\theta, t) \tag{31}$$

where P is the unknown parameter, and $C(\theta, t)$ is a trial function that was estimated by the knowledge of the area occupied by the coil and the magnetic flux concentrator (-15° $\leq \theta \leq$ 15°), and the electrical power of the induction heater over time W_{ind}

$$C(\theta, t) = \begin{cases} W_{ind}(t) & \text{if } \theta \leq 15^\circ \\ 0 & \text{if } \theta > 15^\circ \end{cases} \tag{32}$$

As stated above, the aim of the inverse problem is to determine the unknown parameter P from the wall temperature measurements at $r = r_o$ and at different circumferential positions, denoted as $Y_{r=r_o,\theta=\theta_m}$. Therefore, the solution of the inverse problem is to minimize the following functional:

$$J[P] = \sum_{m=1}^{M_n} \int_{t=0}^{t_f} (T_{r=r_o,\theta=\theta_m} - Y_{r=r_o,\theta=\theta_m})^2 dt \tag{33}$$

where M_n is the total number of temperature sensors (see Figure 3), t_f is the total time in which the experimental measurements are acquired, and $T_{r=r_o,\theta=\theta_m}$ is the numerical solution at measurement positions obtained from the direct problem, which was previously calculated by using an estimated heat flux $q^k_{ind_{r=r_o}}$.

3.2.1. Sensitivity problem

The sensitivity function $\Delta T = \Delta T(r, \theta, t)$, which is the solution of the sensitivity problem, is defined as the directional derivative of the temperature T in the direction of the perturbation of the unknown function (Alifanov, 1994). The sensitivity problem can be formulated by assuming that when the unknown $q_{ind_{r=r_o}}$ is perturbed by $\Delta q_{ind_{r=r_o}}$, then T is perturbed by ΔT. Therefore, replacing $q_{ind_{r=r_o}}$ by $(q_{ind_{r=r_o}} + \Delta q_{ind_{r=r_o}})$ and T by $(T + \Delta T)$ in the direct problem, and subtracting the direct problem from the resulting expressions, the heat diffusion equation for the sensitivity problem is obtained:

$$\rho\, c_p \frac{\partial \Delta T}{\partial t} = \frac{k}{r}\frac{\partial}{\partial r}\left(r\,\frac{\partial \Delta T}{\partial r}\right) + \frac{k}{r^2}\frac{\partial^2 \Delta T}{\partial \theta^2} \tag{34}$$

The boundary and the initial conditions of the sensitivity problem are expressed as follows:

$$k\frac{\partial \Delta T}{\partial r} = h_i\, \Delta T \,\text{at}\; r = r_i \tag{35}$$

$$k\frac{\partial \Delta T}{\partial r} = -h_{conv+rad}\, \Delta T + \Delta q_{ind} \,\text{at}\; r = r_o \tag{36}$$

$$\frac{\partial \Delta T}{\partial \theta} = 0 \,\text{at}\; \theta = 0,\, \pi \tag{37}$$

$$\Delta T = 0 \,\text{for}\; t = 0 \tag{38}$$

where Δq_{ind} is defines as follows

$$\Delta q_{ind} = \Delta P \cdot C(\theta, t) \tag{39}$$

The sensitivity problem was solved in the same manner as that for the direct problem.

3.2.2. Adjoint problem

As stated above, the objective of the inverse problem is to minimize Equation (33), considering that T has to satisfy the direct problem. A Lagrange multiplier $\lambda = \lambda(r, \theta, t)$, which is necessary to obtain the gradient of Equation (33), was obtained by solving the adjoint problem, which consists of multiplying Equation

(1) by λ and integrating the expression over space and time. The resulting expression is then added to Equation (33) to obtain

$$\begin{aligned} J[P] = \sum_{m=1}^{M_n} \int_{t=0}^{t_f} (T_{r=r_o,\theta=\theta_m} - Y_{r=r_o,\theta=\theta_m})^2 dt + \\ \int_{t=0}^{t_f} \int_{r_i}^{r_o} \int_0^{\pi} \lambda \left(\frac{k}{r} \frac{\partial}{\partial r} \left(r \frac{\partial T}{\partial r} \right) + \frac{k}{r^2} \frac{\partial^2 T}{\partial \theta^2} - \rho \, c_p \frac{\partial T}{\partial t} \right) r \, d\theta \, dr \, dt \end{aligned} \tag{40}$$

For obtaining the variation of the functional $\Delta J[P]$, $q_{ind_{r=r_o}}$ was perturbed by $\Delta q_{ind_{r=r_o}}$ and T was perturbed by ΔT, and then Equation (40) was subtracted from the resulting expression:

$$\begin{aligned} \Delta J[P] = \sum_{m=1}^{M_n} \int_{t=0}^{t_f} \int_0^{\pi} 2 \, (T_{r=r_o,\theta=\theta_m} - Y_{r=r_o,\theta=\theta_m}) \Delta T \, \delta(\theta - \theta_m) \, r_o \, d\theta \, dt + \\ \int_{t=0}^{t_f} \int_{r_i}^{r_o} \int_0^{\pi} \lambda \left(\frac{k}{r} \frac{\partial}{\partial r} \left(r \frac{\partial \Delta T}{\partial r} \right) + \frac{k}{r^2} \frac{\partial^2 \Delta T}{\partial \theta^2} - \rho \, c_p \frac{\partial \Delta T}{\partial t} \right) r \, d\theta \, dr \, dt \end{aligned} \tag{41}$$

where $\delta(\cdot)$ is the Dirac function. Integrating the term involving the second derivative in the radial direction by parts and using the boundary conditions of the sensitivity problem (Equations (35) and (36)), the following result is obtained:

$$\begin{aligned} \int_{r_i}^{r_o} k \, \lambda \frac{\partial}{\partial r} \left(r \frac{\partial \Delta T}{\partial r} \right) dr = r_o \, \lambda_{r=r_o} \, \Delta q_{ind_{r=r_o}} - \left(h_{conv+rad} \, \lambda_{r=r_o} + k \frac{\partial \lambda_{r=r_o}}{\partial r} \right) r_o \, \Delta T_{r=r_o} + \\ \left(-h_i \, \lambda_{r=r_i} + k \frac{\partial \lambda_{r=r_i}}{\partial r} \right) r_i \, \Delta T_{r=r_i} + \int_{r_i}^{r_o} k \frac{\partial}{\partial r} \left(r \frac{\partial \lambda}{\partial r} \right) \Delta T \, dr \end{aligned} \tag{42}$$

Integrating by parts the term of Equation (41) involving the second derivative in the circumferential direction and using the boundary conditions of the sensitivity problem (Equation (37)), the following expression is obtained:

$$\int_0^{\pi} k \, \frac{\lambda}{r} \frac{\partial^2 \Delta T}{\partial \theta^2} \, d\theta = \frac{k}{r} \frac{\partial \lambda_{\theta=0}}{\partial \theta} \, \Delta T_{\theta=0} - \frac{k}{r} \frac{\partial \lambda_{\theta=\pi}}{\partial \theta} \, \Delta T_{\theta=\pi} + \int_0^{\pi} \frac{k}{r} \frac{\partial^2 \lambda}{\partial \theta^2} \, \Delta T \, d\theta \tag{43}$$

Integrating by parts the term of Equation (41) involving the derivative in time and using the initial condition of the sensitivity problem (Equation (38)), we obtain

$$\int_0^{t_f} \rho\, c_p\, \lambda\, r \frac{\partial \Delta T}{\partial t}\, dt = \rho\, c_p\, r\, \lambda_{t=t_f}\, \Delta T_{t=t_f} - \int_0^{t_f} \rho\, c_p\, r \frac{\partial \lambda}{\partial t} \Delta T\, dt \qquad (44)$$

Substituting Equations (42)-(44) into Equation (41), the following expression for the variation of the functional is obtained:

$$\begin{aligned}
\Delta J[P] = & \int_{t=0}^{t_f} \int_{r_i}^{r_o} \int_0^{\pi} \left(k\, \frac{\partial}{\partial r} \left(r\, \frac{\partial \lambda}{\partial r} \right) + \frac{k}{r} \frac{\partial^2 \lambda}{\partial \theta^2} + \rho\, c_p\, r \frac{\partial \lambda}{\partial t} \right) \Delta T\, d\theta\, dr\, dt + \\
& \int_{t=0}^{t_f} \int_0^{\pi} \left(-h_i\, \lambda_{r=r_i} + k \frac{\partial \lambda_{r=r_i}}{\partial r} \right) r_i\, \Delta T_{r=r_i}\, d\theta\, dt + \\
& \int_{t=0}^{t_f} \int_0^{\pi} \left(-\, h_{conv+rad}\, \lambda_{r=r_o} - k \frac{\partial \lambda_{r=r_o}}{\partial r} + \sum_{m=1}^{M_n} 2\, (T_{r=r_o} - Y_{r=r_o})\, \delta(\theta - \theta_m) \right) r_o\, \Delta T_{r=r_o}\, d\theta\, dt + \\
& \int_{t=0}^{t_f} \int_{r_i}^{r_o} \frac{k}{r} \frac{\partial \lambda_{\theta=0}}{\partial \theta}\, \Delta T_{\theta=0}\, dr\, dt - \int_{t=0}^{t_f} \int_{r_i}^{r_o} \frac{k}{r} \frac{\partial \lambda_{\theta=\pi}}{\partial \theta}\, \Delta T_{\theta=\pi}\, dr\, dt - \\
& \int_{r_i}^{r_o} \int_0^{\pi} \rho\, c_p\, r\, \lambda_{t=t_f}\, \Delta T_{t=t_f}\, d\theta\, dr + \int_{t=0}^{t_f} \int_0^{\pi} r_o\, \lambda_{r=r_o}\, \Delta q_{ind_{r=r_o}}\, d\theta\, dt
\end{aligned} \qquad (45)$$

The adjoint problem equations for determining λ are obtained by eliminating the six first integral terms containing ΔT in Equation (45)

$$k\, \frac{\partial}{\partial r} \left(r\, \frac{\partial \lambda}{\partial r} \right) + \frac{k}{r} \frac{\partial^2 \lambda}{\partial \theta^2} + \rho\, c_p\, r \frac{\partial \lambda}{\partial t} = 0 \qquad (46)$$

$$\begin{aligned}
k \frac{\partial \lambda}{\partial r} &= h_i\, \lambda \,\text{at}\; r = r_i & (47)\\
k \frac{\partial \lambda}{\partial r} &= -h_{conv+rad}\, \lambda + \sum_{m=1}^{M_n} 2\, (T_{r=r_o} - Y_{r=r_o}\, \delta(\theta - \theta_m) \,\text{at}\; r = r_o & (48)\\
\frac{\partial \lambda}{\partial \theta} &= 0 \,\text{at}\; \theta = 0,\, \pi & (49)\\
\lambda &= 0 \,\text{for}\; t = t_f & (50)
\end{aligned}$$

The adjoint problem is different from the direct problem because the condition at $t = t_f$ is known rather than knowing the condition at $t = 0$, but both problems can be solved in the same manner by changing the time variable as $\tau = t_f - t$ for solving the adjoint problem.

After leading the six first integral terms of Equation (45) to vanish, the following expression for ΔJ remains:

$$\Delta J[P] = \int_{t=0}^{t_f} \int_0^{\pi} \lambda_{r=r_o} \, \Delta q_{ind_{r=r_o}} \, r_o \, d\theta \, dt \tag{51}$$

By substituting (39) into (51)

$$\Delta J[P] = \int_{t=0}^{t_f} \int_0^{\pi} \lambda_{r=r_o} \, C \, \Delta P \, r_o \, d\theta \, dt \tag{52}$$

The definition of the direction derivative of $J[P]$ in the direction of a vector ΔP is

$$\Delta J[P] = \nabla J[P] \, \Delta P \tag{53}$$

Comparing Equations (52) and (53), the gradient equation for the functional is obtained:

$$\nabla J[P] = J'[P] = \int_{t=0}^{t_f} \int_0^{\pi} \lambda_{r=r_o} \, C \, r_o \, d\theta \, dt \tag{54}$$

3.2.3. Conjugate gradient method

The iterative procedure to obtain P by minimizing the functional $J[P]$ is based on the conjugate gradient method. The unknown parameter P at the kth iteration is estimated following the expression

$$P^{k+1} = P^k - \beta^k \, d^k \tag{55}$$

where β^k is the search step size and d^k is the direction of descent

$$d^k = J'[P^k] + \gamma^k \, d^{k-1} \tag{56}$$

where γ^k is the conjugation coefficient and is calculated with the following expression:

$$\gamma^k = \frac{(J'[P^k])^2}{(J'[P^{k-1}])^2} \quad \text{with } \gamma^0 = 0 \tag{57}$$

The step size β^k is calculated by minimizing the functional $J[P^{k+1}]$ with respect to β^k. The functional $J[P^{k+1}]$ is expressed following Equation (33) as

$$J[P^{k+1}] = \sum_{m=1}^{M_n} \int_{t=0}^{t_f} \left[T_{r=r_o,\theta=\theta_m}(P^k - \beta^k \, d^k) - Y_{r=r_o,\theta=\theta_m} \right]^2 dt \tag{58}$$

Linearizing $T(P^k - \beta^k\, d^k)$ by a Taylor expansion and minimizing the resulting expression with respect to β^k, the following result is obtained:

$$\beta^k = \frac{\sum_{m=1}^{M_n} \int_{t=0}^{t_f} \left[(T_{r=r_o,\theta=\theta_m}(P^k) - Y_{r=r_o,\theta=\theta_m})\, \Delta T(d^k) \right] dt}{\sum_{m=1}^{M_n} \int_{t=0}^{t_f} \left[\Delta T(d^k) \right]^2\, dt} \tag{59}$$

where $T_{r=r_o,\theta=\theta_m}(P^k)$ is the solution of the direct problem at the measured locations $\theta = \theta_m$ by using the estimated P^k, and $\Delta T(d^k)$ is the solution of the sensitivity problem at $\theta = \theta_m$ by using $\Delta P = d^k$.

3.2.4. Stopping criterion

The stopping criterion is based on the discrepancy principle, which means that the procedure is stopped when the functional becomes lower than the variance of the measurement errors:

$$J[P] < M_n\, \sigma^2\, t_f \tag{60}$$

where M_n is the number of thermocouples welded to the outer surface of the wall (5 in this case), and σ is the standard deviation of the measurement errors, which is considered to be 8°C for the experiments accomplished in this work.

3.2.5. Iterative procedure

In this section, the computational algorithm to solve the inverse problem is summarized. Suppose that P^k is known at iteration k.

1. Compute q_{ind} according to Equation (31) and solve the direct problem (Equations (1)-(5)) to obtain T.
2. Check the stopping criterion (Equation (60)) and continue if it is not satisfied.
3. Solve the adjoint problem (Equations (46)-(50)) to obtain λ.
4. Calculate the gradient of the functional $J'[P]$ from Equation (54).
5. Calculate the direction of descent d^k and the conjugate coefficient γ^k from Equations (56) and (57).
6. Determine $\Delta P = d^k$, compute Δq_{ind} from Equation (39) and solve the sensitivity problem (Equations (34)-(38)) to obtain ΔT.

7. Calculate the search step size β^k (Equation (59)).
8. Calculate the new estimation P^{k+1} from Equation (55) and return to step 1.

3.3. Solution procedure

The governing equations of the inverse problem were numerically solved using a finite difference method, with mesh sizes of $\Delta r = 0.4$ mm and $\Delta\theta = 5°$. A fourth-order Runge-Kutta formulation was performed to solve the transient problem. The numerical model was written in MATLAB software, and the simulations were conducted with an Intel(R)Core(TM) i7-4790 3.60 GHz CPU. The relative error between the measurements of the external wall temperature of the tube and the numerical results obtained from the inverse problem reached a maximum value of 10% when the heat flux abruptly changes at $t = 50$ s and $t = 350$ s, as the induction coil starts heating and stops heating the pipe, respectively. The relative error between calculated and measured temperature when the heat flux provided by the induction heater is maximum is approximately 1%. Besides, the deflection of the tube caused by the unilateral heat flux was calculated from the radial temperature profile obtained with the inverse method, and it was compared with the measured deflection. The maximum difference between the measured and calculated displacements was 0.3 mm, which is considered acceptable because the measurement resolution is 0.4 mm. Code verification is defined as a set of methods developed to find coding mistakes that affect the numerical discretization. In this case, code verification of the direct problem was evaluated with the method of exact solutions (Roy, 2005; ASME, 2009), which consists of contrasting the numerical solution to an exact solution of the partial differential equations with specified initial and boundary conditions. In particular, the wall temperature numerical solution at a time sufficiently large for the temperature evolutions to reach steady state is compared with the solution published by Holms (1952) and compiled by Logie et al. (2018) to the two-dimensional steady-state conduction in a hollow cylinder subjected to asymmetrical temperature distributions at the external boundary. For comparison to the analytical solution, the boundary conditions for the numerical direct problem were fixed to a known constant temperature at $r = r_i$, and known variable heat flux in azimuthal direction at $r = r_o$ taken from the derivative expression of the temperature distribution. Negligible differences between the wall temperature numerical results and the analytical solution were observed, with a relative error of 0.02%. Furthermore, to verify that the transient response of the wall temperature is accurately solved, the numerical solution is compared to the analytical solution from Hahn and Özisik (2012) for the wall temperature evolution with time of a long hollow cylinder maintained at a constant temperature of 0 °C at inner and outer surfaces. In this case, the wall temperature is only dependent on radial direction and time, and not dependent on azimuthal direction. The maximum relative error between both numerical and analytical temperature results is lower than 1%.

In this work, the sensitivity of the calculated heat flux to changes in outer surface temperature measurements, molten salt-to-wall heat transfer coefficient, and angular position of the thermocouples has been calculated. Being the standard deviation of the temperature measurements 8 °C, the uncertainty in the calculated heat flux is 15 kW/m^2, which corresponds to a 2% of the obtained heat flux. The standard uncertainty of molten salt-to-wall heat transfer coefficient was considered to be 20% due to the uncertainties in the molten salt thermophysical properties, the molten salt velocity measured with the flow meter, and the experimental correlation used. The uncertainty in the heat flux due to the uncertainty in the molten salt-to-wall heat transfer coefficient is 87 kW/m^2 (10% of the calculated heat flux). Finally, the uncertainty in the angular position of the thermocouples is 5°, caused by the slight descend of the pipe due to the molten salt flow during the experiments. The uncertainty in the heat flux due to the uncertainty in the angular position of the thermocouples is 120 kW/m^2, which is 15% of the obtained heat flux.

4. Results and discussion

As stated above, the main goal of this work is to obtain the unknown heat flux received by the pipe from the external wall temperature measurements by solving the inverse problem. Four different experiments were conducted, varying the molten-salt velocity and the heating rate of the induction coil, as shown in Table 1. Figure 8 shows the heat flux evolution with time using the inverse method. Experiments 2, 3 and 4 were conducted following the same heating sequence over time: during the first 50 seconds, the inductor is not heating the tube; for the next 5 minutes, the inductor provides 4 kW_e of power for heating the tube. Finally, during the last minute, the inducer switches off. In the first experiment, the heating process starts at $t = 50$ s, the power linearly increases up to the value of 4 kW_e over the course of 2 minutes, it remains constant for 1 minute, and then it linearly decreases for 2 minutes until the induction heater switches off. As shown in Figure 8, the maximum heat flux generated by the induction heater (at t=200 s), which corresponds to 4 kW_e of power, is 765 kW/m^2 for Experiment 1, 800 kW/m^2 for Experiment 2, 865 kW/m^2 for Experiment 3, and 930 kW/m^2 for Experiment 4. Therefore, we concluded that approximately 28-34% of the electric power of the induction heater is converted to thermal energy that reaches the tube, which is slightly lower than the results of 40% electric-to-thermal efficiency obtained during the calibration of the induction heater. Notice that, although the electric power of the inductor was 4 kW_e for all the experiments, the heat flux received by the pipe varied from one experiment to another, because it is affected by some parameters difficult to control during the experiments, such as the distance between the coil and the pipe, and the inlet and outlet temperatures of the inductor cooling water.

[Figure 8 about here.]

Figure 9 shows the comparison between the external pipe temperatures obtained using the inverse method (solid lines) and the external pipe temperature measurements (markers) at different angular positions for the different experiments. Regarding the molten-salt velocity, Figures 9 a) and b) for a velocity of 0.78 m/s show higher temperatures in the front side of the tube in comparison with Figures 9 c) and d) for velocities of 1.21 and 2.89 m/s because the increase in velocity enhances the heat transfer such that the wall temperature is reduced. As shown, the temperatures obtained with the inverse method accurately fit the experimental measurements. The maximum relative error for the angular position corresponding to $\theta = 12.5°$ is approximately 10% for experiment 4 when the heat flux abruptly changes at t=50 s and t=350 s, as the induction coil starts heating and stops heating the pipe, respectively. The relative error between calculated and measured temperature when the heat flux provided by the induction heater is maximum is approximately 1%.

[Figure 9 about here.]

Figure 10 shows the temperature profiles along the circumferential and radial positions and the heat flux profile along circumferential direction at $t = 200$ s. As shown, the maximum temperature corresponds to the center of the coil $\theta = 0°$; then, the temperature decreases, where the derivative with respect to the angular position is higher from $\theta = 0°$ to $\theta = 30°$. Finally, the temperature remains nearly constant from $\theta = 60°$. It is shown that lower molten-salt velocities result in higher temperatures at the front side of the tube and thus a greater temperature difference between the front and rear side of the tube.

Equations (31) and (32) establish that the heat flux is a step-function in the circumferential direction, as it is shown in Figure 10, where the surface of the pipe facing the induction coil that is reached by the heat flux spans from $\theta = -15°$ to $\theta = 15°$.

[Figure 10 about here.]

The accuracy of the radial temperature profile can be verified by comparing the displacement of the pipe obtained using Equations (28)-(30) with the experimental measurements using the camera, as shown in Figure 11. The maximum difference between the measured and calculated displacements is 0.3 mm for experiment 1 at t=80 s and t=330 s. At those moments is when the deviation between the measured and modeled temperature difference between the rear and front side is higher. Because the measurement resolution is 0.4 mm, the difference between the numerical results and measurements is considered acceptable. As shown in Figure 11, lower molten-salt velocities result in higher displacement of the pipe because the temperature difference between the front and rear sides of the tube is greater.

[Figure 11 about here.]

4.1. Influence of the convective heat transfer coefficient between the molten salt and the pipe wall

In this section, the influence of the convective heat transfer coefficient from the molten salt to the inner wall on the temperatures distribution along the cross section of the pipe was studied. Differences of 20% between convective heat transfer results obtained using different correlations for forced convective heat transfer in straight tubes proposed by Cheesewright et al. (1992) were found in the range of Reynolds and Prandtl numbers used in this work. Therefore, different convective heat transfer coefficients h_i coming from the products of the value from the correlation proposed by Petukhov (1970) and the scale factor of 0.8 were tested. As shown in Figure 12, keeping the temperature of the external wall fixed, higher convective heat transfer coefficients result in lower temperatures in the internal wall. A variation of 20% in the convective heat transfer results in a variation of 10% in the heat flux obtained with the inverse method.

[Figure 12 about here.]

5. Conclusions

An inverse method has been used to obtain the unknown time-dependent heat flux received by a pipe with a flow of molten nitrate salt at a temperature of approximately 430 °C from outer surface temperature measurements. The measurements were performed in a molten salt test loop at realistic operational conditions of a solar tower receiver. The external surface of the pipe in the measurement area was heated using an induction heater, which provided a very high nonuniform heat flux that can be estimated based on the electric power provided by the induction heater, but it cannot be measured with accuracy.

A set of experiments in which the molten-salt velocity and heating rate were varied were conducted to obtain outer surface temperature measurements along the circumferential direction for both the front and rear sides of the tube. Lower molten-salt velocities resulted in higher temperatures at the front side of the tube and therefore a greater temperature difference between the front and rear sides of the tube because the convective heat transfer coefficient from the molten salt to the wall increases with molten-salt velocity.

To solve the inverse problem, a transient numerical model of a circular pipe conducting molten nitrate salt and subjected to a nonhomogeneous heat flux was developed. A two-dimensional model in radial and circumferential directions was proposed, as thermal conduction in axial direction was shown to be negligible. Once the heat flux was obtained from the outer surface temperature measurements by means of the inverse method, the radial temperature profile in the pipe wall was obtained. Furthermore, the deflection of the tube caused by the unilateral heat flux was measured, and it was compared to the deflection calculated from the radial temperature profile.

The outer surface temperature results obtained using the inverse method exhibited good agreement with the experimental measurements, as the maximum relative error is approximately 10% for experiment 4 when the heat flux abruptly changes at t=50 s and t=350 s, as the induction coil starts heating and stops heating the pipe, respectively. The relative error between calculated and measured temperature when the heat flux provided by the induction heater is maximum is approximately 1%. The heat flux estimated using the inverse heat transfer method was in the range 765-930 kW/m^2 in the different experiments. These values are in accordance with the heat flux that the inductor provides according to the calibration experiments conducted. Regarding the tube bending, the maximum difference between the measured and calculated displacements of the tube was 0.3 mm, which was considered acceptable as the resolution of the measurement was 0.4 mm; thus, the accuracy of the radial temperature profile of the pipe obtained with the inverse method was verified.

Acknowledgments This work was partially funded by the Ministerio de Eduación, Cultura y Deporte para la Formación de Profesorado Universitario (FPU-04941), the Ministerio de Economía y Competitividad (Project ENE2015-69486-R(MINECO,FEDER,UE) and Project ENE2016-78908-R) of the Spanish Government and the Project SBPLY/17/180501/000412 of the Regional Government of Castilla-La Mancha. Assistance provided by D. Diaz, I. Pina and M. Santos with the experimental installation was greatly appreciated.

6. Notation

c_p Specific heat [J/(kg K)]

C Trial function [W/m^2]

d Direction of descent [W/m^2]

d_i Internal diameter of the tube [m]

E Modulus of elasticity [GPa]

h_i Convective heat transfer coefficient between the molten salt and pipe wall [W/(m^2 K)]

$h_{conv+rad}$ Mixed convective and radiative heat transfer coefficient from the outer surface of the pipe to the atmosphere [W/(m^2 K)]

h_∞ Convective heat transfer coefficient between the air and the pipe [W/(m^2 K)]

I Moment of inertia [m^4]

J Inverse problem functional [$K^2\, s$]

k Thermal conductivity [W/(m K)]

K Conductance [W/K]

L Cell length [m]

L_T Total length of the tube [m]

N_k Number of nodes in circumferential direction [-]

M Bending moment [N m]

M_k Number of nodes in radial direction [-]

M_T Moment induced by circumferential temperature gradient [N m]

M_n Number of measurements [-]

Re Reynolds number, $Re = \frac{\rho_s\, u\, d_i}{\mu_s}$ [-]

P Unknown parameter, [-]

Pr Prandtl number, $Pr = \frac{\mu_s\, c_{p,s}}{k_s}$ [-]

q_{ind} Heat flux generated by induction heater received by the tube [W/m^2]

Q Heat flow [W]

R Reaction force [N]

r Radius [m]

r_i Inner tube radius [m]

r_o Outer tube radius [m]

t Time [s]

t_f Total duration of the experiments [s]

T Wall temperature [°C]

T_s Molten-salt temperature [°C]

T_∞ Surroundings temperature [°C]

u Molten salt velocity [m/s]

V Cell volume [m^3]

W_{ind} Electrical power of the induction heater [W]

Y Measured temperature [°C]

z Axial direction [m]

6.1. Greek symbols

α Thermal expansion coefficient [K^{-1}]

β Search step size [-]

δ Deflection of the tube [m]

γ Conjugation coefficient [-]

ΔT Sensitivity function [K]

Δr Increment in radial direction [m]

$\Delta\theta$ Increment in circumferential direction [m]

ε Emissivity [-]

λ Adjoint function [-]

μ Molten salt viscosity[Pa/,s]

ρ Density [kg/m^3]

σ_r Stefan-Boltzmann constant, 5.67×10^{-8} [W/(m^2 K^4)]

Θ Rotation of the tube [-]

θ Circumferential location [-]

τ Transformed time coordinate [s]

6.2. Subscripts

i Node number along the circumferential direction

j Node number along the radial direction

s Molten salt

6.3. Superscripts

k Number of iteration

References

Alifanov, O. M., 1994. Inverse Heat Transfer Problems. Springer-Verlag.

ASME, 2009. V&V 20-2009: Standard for verification and validation in computational fluid dynamics and heat transfer.

Cattani, L., Maillet, D., Bozzoli, F., Rainieri, S., 2015. Estimation of the local convective heat transfer coefficient in pipe flow using a 2D thermal Quadrupole model and Truncated Singular Value Decomposition. International Journal of Heat and Mass Transfer 91, 1034–1045.

Cheesewright, R., Heeggs, P. J., Martin, B. W., Parry, W. J., Ralston, T., 1992. Forced convection heat transfer in straight tubes. Tech. Rep. 92003, Engineering Science Data Unit.

Churchill, S. W., Chu, H. H. S., 1975. Correlating equations for laminar and turbulent free convection from a horizontal cylinder. International Journal of Heat and Mass Transfer 18, 1049–1058.

Du, B.-C., He, Y.-L., Wang, K., Zhu, H.-H., 2017. Convective heat transfer of molten salt in the shell-and-tube heat exchanger with segmental baffles. International Journal of Heat and Mass Transfer 113, 456–465.

Duarte, J. P., Zhao, D., Jo, H., Corradini, M. L., 2018. Critical heat flux experiments and a post-CHF heat transfer analysis using 2D inverse heat transfer. Nuclear Engineering and Design 337, 17–26.

Gao, K., Qin, X., Wang, Z., Zhu, S., Gan, Z., 2016. Effect of magnetizer geometry on the spot induction heating process. Journal of Materials Processing Technology 231, 125–136.

Gere, J. M., 2004. Mechanics of materials. Thomson Learning.

Hafid, M., Lacroix, M., 2017. Inverse heat transfer prediction of the state of the brick wall of a melting furnace. Applied Thermal Engineering 110, 265–274.

Hahn, D. W., Özisik, M. N., 2012. Heat conduction, 3rd Edition. John Wiley & Sons, Inc.

Holms, A. G., 1952. A Biharmonic Relaxation Method for Calculating Thermal Stress in Cooled Irregular Cylinders. Tech. Rep. NACA-TR-1059, Lewis Flight Propulsion Lab.

Jianfeng, L., Xiangyang, S., Jing, D., Qiang, P., Yuliang, W., 2013a. Convective heat transfer of high temperature molten salt in transversely grooved tube. Applied Thermal Engineering 61, 157–162.

Jianfeng, L., Xingyang, S., Jing, D., Jianping, Y., 2013b. Transition and turbulent convective heat transfer of molten salt in spirally grooved tube. Experimental Thermal Fluid Science 47, 180–185.

Kim, H., Kim, H., Lee, S., Kim, J., 2018. A study on heat transfer characteristics of quinary molten salt mixture. International Journal of Heat and Mass Transfer 127, 465–472.

Kruizenga, A. M., Kolb, W., Briggs, R. J., Chistian, J., Ray, D., Gill, D., Kelton, J., Chisman, K., 2014. Loop for the Observation of Film Temperature Effects on Descomposition (LOFTED). Tech. Rep. SAND2014-18103, Sandia National Laboratories.

Liu, T., Montefort, J., Standfield, S., Palluconi, S., Crafton, J., Cai, Z., 2018. Analytical inverse heat transfer method for temperature-sensitive-coating measurement on a finite base. International Journal of Heat and Mass Transfer 118 118, 651–662.

Logie, W. R., Pye, J. D., Coventry, J., 2018. Thermoelastic stress in concentrating solar receiver tubes: A retrospect on stress analysis methodology, and comparison of salt and sodium. Solar Energy 160, 368–379.

Lu, T., Liu, B., Jian, P., Zhang, Y., Li, H., 2010. A two-dimensional inverse heat conduction problem in estimating the fluid temperature in a pipeline. Applied Thermal Engineering 30, 1574–1579.

Maillet, D., Degiovanni, A., Pasquetti, R., 1991. Inverse heat conduction applied to the measurement of heat transfer coefficient on a cylinder: comparison between an analytical and a boundary element technique. Journal of Heat Transfer 113, 549–557.

Marugán-Cruz, C., Flores, O., Santana, D., García-Villalba, M., 2016. Heat transfer and thermal stresses in a circular tube with non-uniform heat flux. International Journal of Heat and Mass Transfer 96, 256–266.

Özisik, M. N., Orlande, H. R. B., 2000. Inverse Heat Transfer. Taylor and Francis.

Pacheco, J. E., 2002. Final Test and Evaluation Results from the Solar Two Project. Tech. Rep. SAND2002-0120, Sandia National Laboratories.

Perakis, N., Haidn, O. J., 2019. Inverse heat transfer method applied to capacitively cooled rocket thrust chambers. International Journal of Heat and Mass Transfer 131, 150–166.

Petukhov, B. S., 1970. Heat transfer and friction in turbulent pipe flow with variable physical properties. Advances in Heat Transfer 6, 503–564.

Reddy, K. S., Premjit, N. S., Somasundharam, S., 2018. In-situ prediction of focal flux distribution for concentrating photovoltaic (CPV) system using inverse heat transfer technique for effective design of receiver. Solar Energy 159, 510–518.

Roy, C. J., 2005. Review of code and solution verification procedures for computational simulation. Journal of Computational Physics 205, 131–156.

Smith, D. C., Chavez, J. M., 1992. A Final Report on the Phase I Testing of a Molten-Salt Cavity Receiver. Tech. Rep. SAND87-2290, Sandia National Laboratories.

Su, J., Silva-Neto, A. J., 2001. Two-dimensional inverse heat conduction problem of source strength estimation in cylindrical rods. Applied Mathematical Modelling 25, 861–872.

Taler, J., Duda, P., 2006. Solving Direct and Inverse Heat Conduction Problems. Springer.

Taler, J., Duda, P., Weglowski, B., Zima, W., Gradziel, S., Sobota, T., Taler, D., 2009. Identification of local heat flux to membrane water-walls in steam boilers. Fuel 88, 305–311.

Taler, J., Taler, D., Ludowski, P., 2014. Measurements of local heat flux to membrane water walls of combustion chambers. Fuel 115, 70–83.

Xiangyang, S., Jianfeng, L., Jing, D., Jianping, Y., 2014. Convective heat transfer of molten salt in circular tube with nonuniform heat flux. Experimental Thermal and Fluid Science 55, 6–11.

Yadav, M. K., Singh, S. K., Parwez, A., Khandekar, S., 2018. Inverse models for transient wall heat flux estimation based on single and multi-point temperature measurements. International Journal of Thermal Sciences 124, 307–317.

Yang, C., Chen, W. L., Chou, H. M., Salazar, J. L. L., 2013. Inverse hyperbolic thermoelastic analysis of a functionally graded hollow circular cylinder in estimating surface heat flux and thermal stresses. International Journal of Heat and Mass Transfer 60, 125–133.

Yang, X., Yang, X., Ding, J., Shao, Y., Fan, H., 2012. Numerical simulation study on the heat transfer characteristics of the tube receiver of the solar thermal power tower. Applied Energy 90, 142–147.

Yu-ting, W., Bin, L., Chong-fang, M., Hang, G., 2009. Convective heat transfer in the laminar-turbulent transition region with molten salt in a circular tube. Experimental Thermal and Fluid Science 33, 1128–1132.

Zavoico, A. B., 2001. Solar Power Tower Design Basis Document. Tech. Rep. SAND87-2290, Sandia National Laboratories.

Zhu, Z., Qin, X., Gao, K., Chen, X., 2018. Design and research on the spot inductor for obtaining local high temperature rapidly. International Communications in Heat and Mass Transfer 96, 122–129.

List of Figures

Figure 1: Photograph of the molten salt test loop.

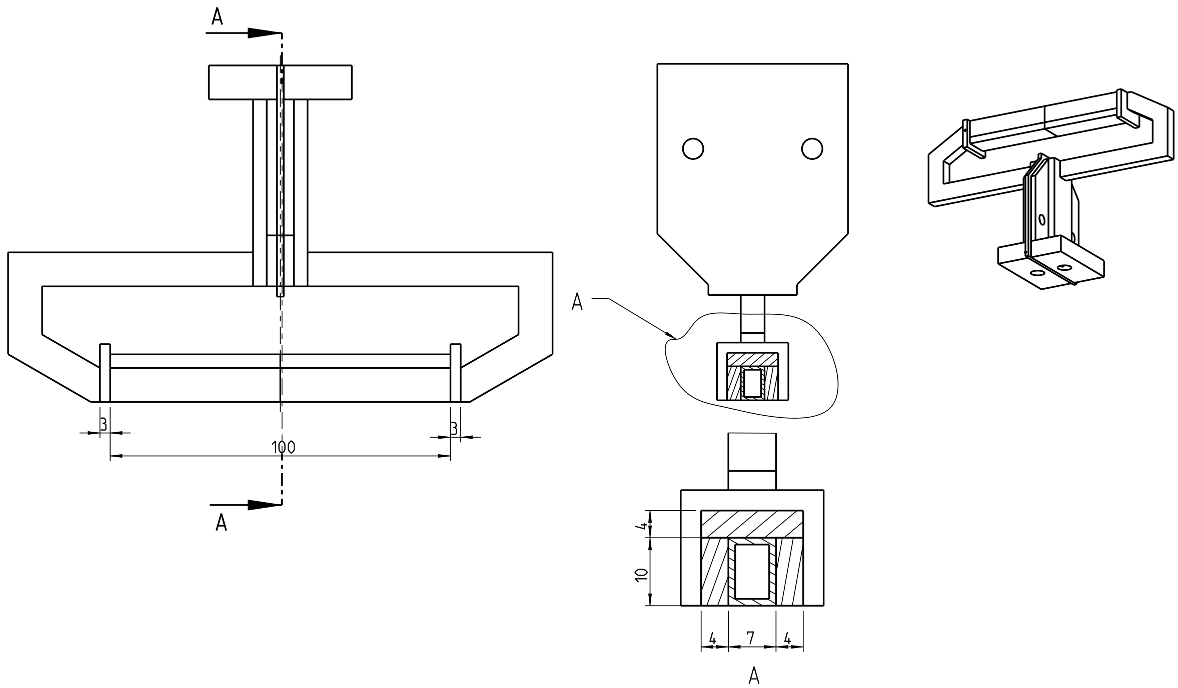

Figure 2: Detail of the induction coil. Dimensions are in mm.

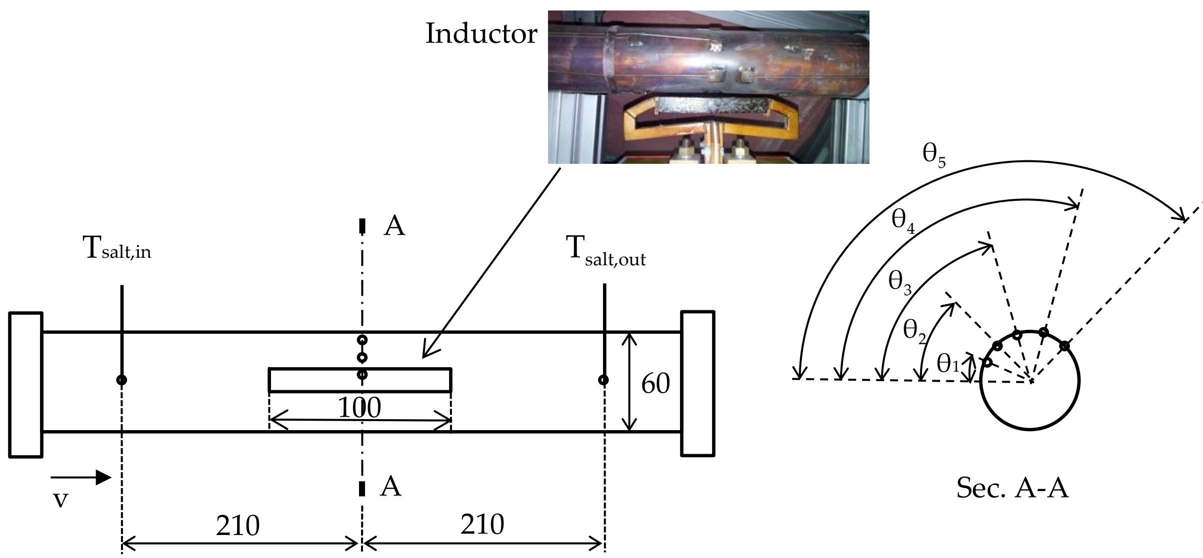

Figure 3: Details of the test section, including the positions of the induction coil and thermocouples. $\theta_1 = 12.5°$, $\theta_2 = 47.5°$, $\theta_3 = 72.5°$, $\theta_4 = 107.5°$, and $\theta_5 = 132.5°$ Dimensions are in mm.

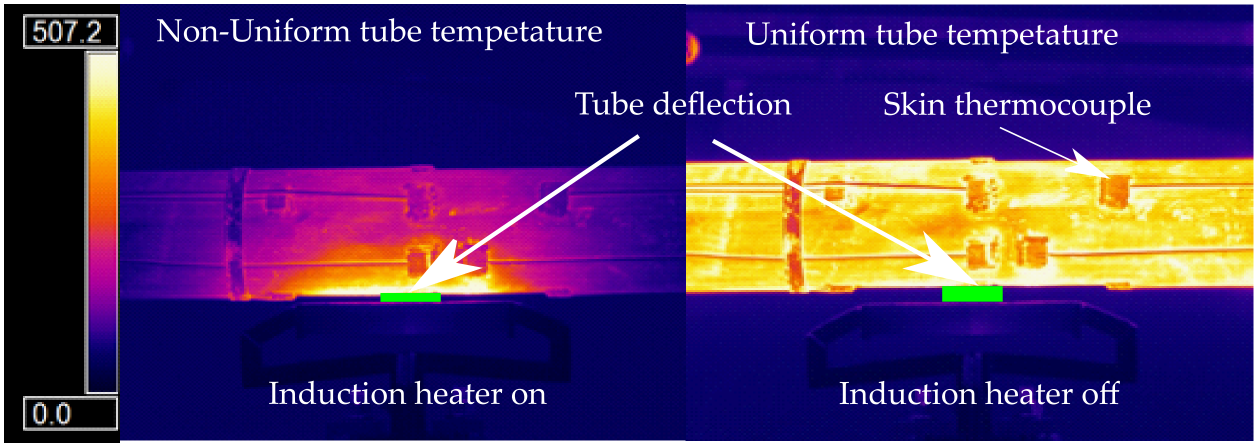

Figure 4: Thermal images for nonuniform tube temperature and uniform tube temperature. Temperatures are in °C.

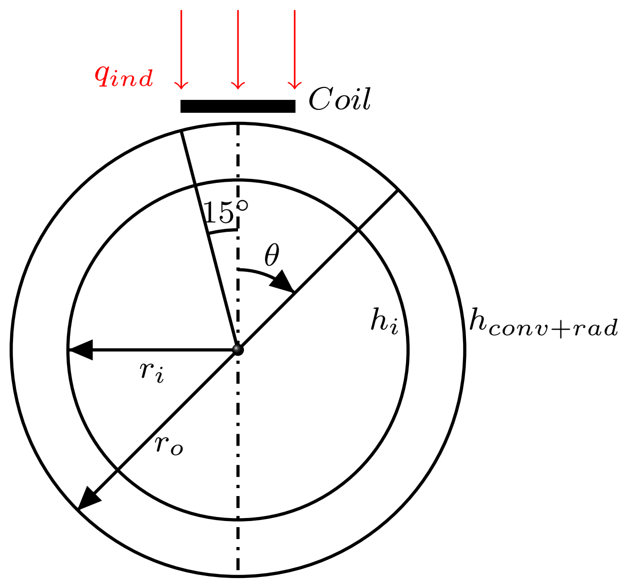

Figure 5: Geometry and coordinate system.

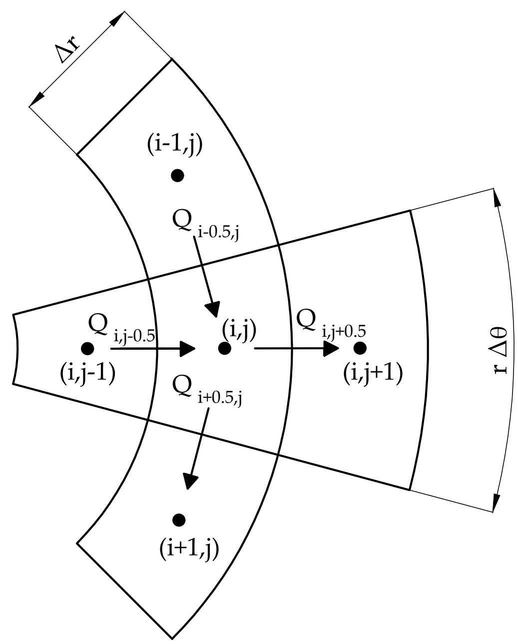

Figure 6: Mesh in cylindrical coordinates. Definitions of heat flows (Q) to and from cell (i,j)

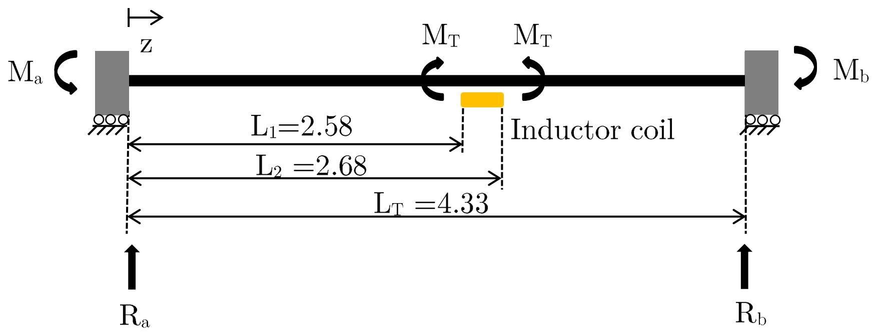

Figure 7: Scheme of the receiver tube (black), induction coil (yellow) and supports along the z axis. Distances are in m.

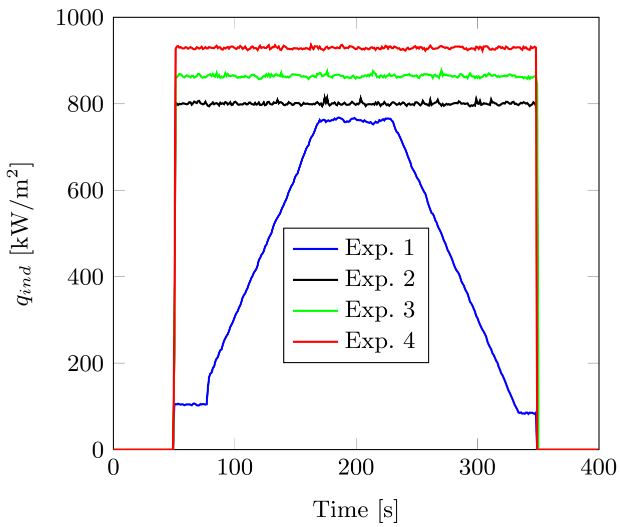

Figure 8: External pipe heat flux evolution with time at $-15° \leq \theta \leq 15°$, obtained using the inverse method.

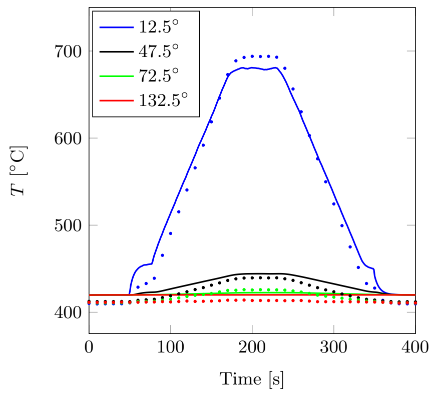

(a) Experiment 1.

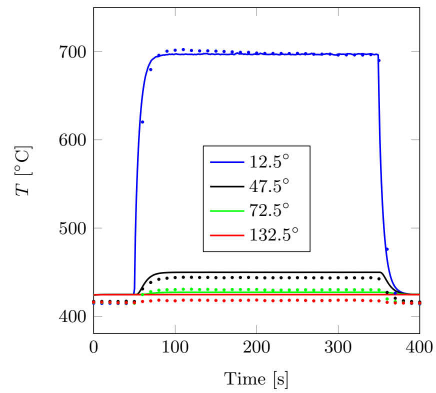

(b) Experiment 2.

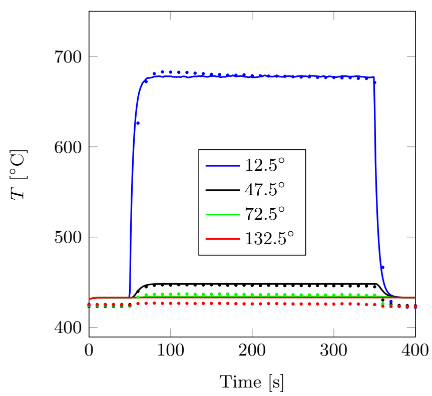

(c) Experiment 3.

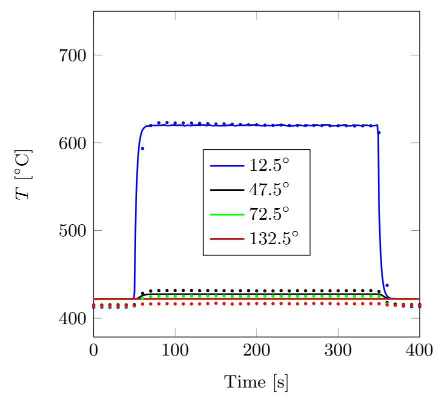

(d) Experiment 4.

Figure 9: Evolution of the external pipe temperatures at different angular positions. Markers correspond to experimental measurements, and solid lines correspond to the results obtained using the inverse method. Measured temperature shown each 10 seconds.

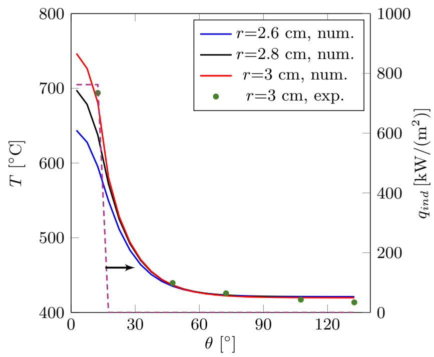

(a) Experiment 1.

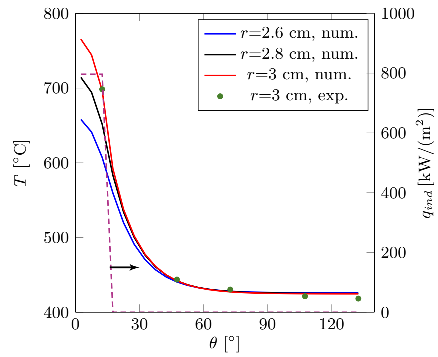

(b) Experiment 2.

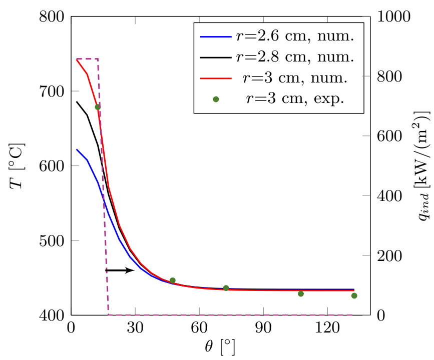

(c) Experiment 3.

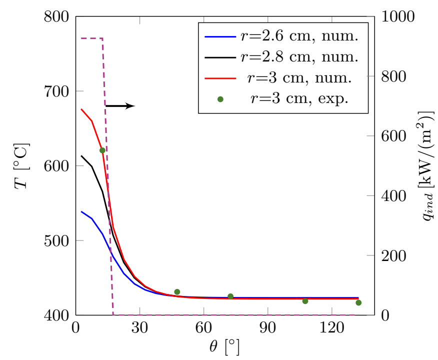

(d) Experiment 4.

Figure 10: Temperature profiles along the circumferential and radial positions at t=200 s from the beginning of the experiment. Purple dashed line shows the heat flux profile along the circumferential positions at t=200 s.

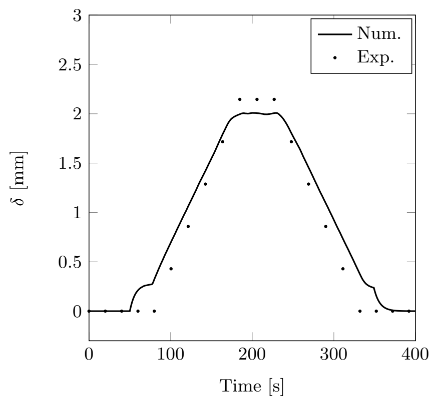

(a) Experiment 1.

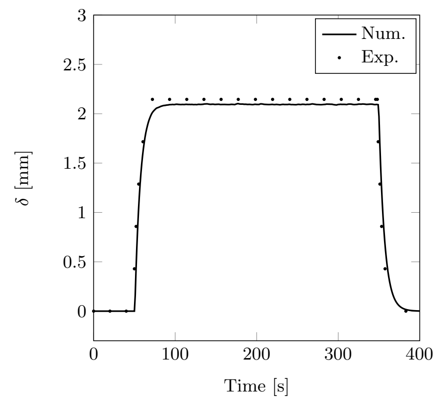

(b) Experiment 2.

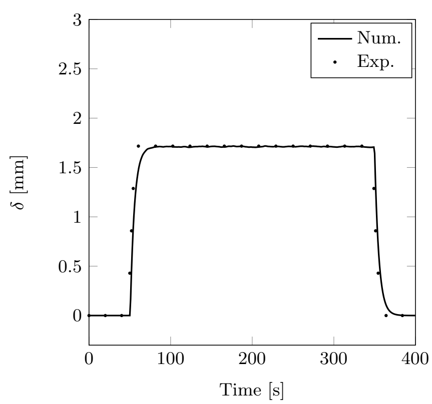

(c) Experiment 3.

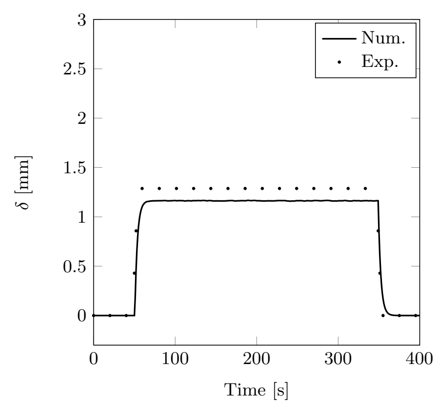

(d) Experiment 4.

Figure 11: Comparison between pipe displacement obtained using the inverse method and pipe displacement measurements using the infrared camera. Measured displacement shown each 20 seconds.

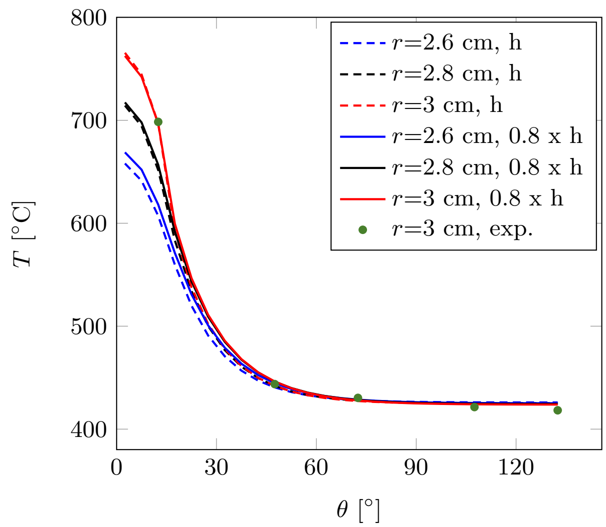

Figure 12: Temperature profiles along the circumferential and radial positions for Experiment 1 for different values of h_i coming from the products of the value from the correlation proposed by Petukhov (1970) and different scale factors: 0.8 x h_w (solid line) and 1 x h_w (dashed line).

List of Tables

	Exp. 1	Exp. 2	Exp. 3	Exp. 4
Heating function	Ramp	Step	Step	Step
Molten-salt inlet velocity, u (m/s)	0.78	0.78	1.22	2.89
$Re = \frac{\rho_s\, u\, d_i}{\mu_s}$ (-)	46897	46977	75002	170985
$Pr = \frac{\mu_s\, c_{p,s}}{k_s}$ (-)	4.64	4.55	4.44	4.63
Molten-salt inlet temperature, T_s (°C)	424.5	429.1	436.1	424.7
Ambient temperature, T_∞ (°C)	34.0	32.9	31.4	34.1

Table 1: Experimental conditions.